JGR Atmospheres

RESEARCH ARTICLE
10.1029/2021JD035961

Special Section:
Years of the Maritime Continent

A Multivariate Index for Tropical Intraseasonal Oscillations Based on the Seasonally-Varying Modal Structures

Shuguang Wang[1], Zane K. Martin[2], Adam H. Sobel[3,4], Michael K. Tippett[3], Juliana Dias[5], George N. Kiladis[5], Hong-Li Ren[6], and Jie Wu[7]

[1]School of Atmospheric Sciences, Key Laboratory of Mesoscale Severe Weather/Ministry of Education, Nanjing University, Nanjing, China, [2]Department of Atmospheric Science, Colorado State University, Fort Collins, CO, USA, [3]Department of Applied Physics and Applied Mathematics, Columbia University, New York, NY, USA, [4]Lamont-Doherty Earth Observatory of Columbia University, Palisades, NY, USA, [5]Physical Sciences Division, NOAA/Earth System Research Laboratory, Boulder, CO, USA, [6]State Key Laboratory of Severe Weather, Chinese Academy of Meteorological Sciences, Beijing, China, [7]Laboratory for Climate Studies & China Meteorological Administration-Nanjing University Joint Laboratory for Climate Prediction Studies, National Climate Center, China Meteorological Administration, Beijing, China

Abstract The spatial structure and propagation characteristics of tropical intraseasonal oscillations vary substantially by season. In this study, these seasonal variations are identified using a multivariate sliding-window Empirical Orthogonal Function (EOF) analysis. The two modes comprising the leading EOF pair have equal variances and depict the propagation of intraseasonal oscillations in convection and low-level circulation over the Indian Ocean, the Maritime Continent, and the western Pacific region in the equatorial summer hemisphere. In contrast, the upper tropospheric circulation shows more structure in the winter hemisphere. It is suggested that this variation in seasonality with height is an inherent feature of intraseasonal oscillations. A new multivariate index for tropical intraseasonal oscillations (MII) is developed based on the leading EOFs and represents the three-dimensional structure of intraseasonal variability in all seasons. The MII is computed by projecting intraseasonal anomalies onto the leading EOFs pair, and it exhibits clearly delineated but smooth seasonal transitions and rich meridional structure. The real-time version of this new index, rMII, is shown to be similar to MII, with a correlation of 0.9. Compared to the widely used Real-time Multivariate MJO (RMM) index, the power spectrum of rMII represents substantially greater intraseasonal variance, and the application of rMII in dynamical forecast models indicates rMII is skillfully predicted for an additional week compared to RMM.

Plain Language Summary The Madden-Julian Oscillation and boreal summer intraseasonal oscillation are the most important oscillations in the tropical atmosphere on the intraseasonal time scale (a few weeks to a couple of months). While they are similar in a number of respects, there are important differences between the two: they are active in different seasons, often display different shapes in weather maps, and move in different directions. An important research question is how to track these oscillations in real-time across all the seasons. Toward this goal, we develop a new machine learning algorithm to automatically identify spatial and temporal patterns of the oscillations in this research. We apply the new algorithm to identify the oscillations in output from state-of-the-art subseasonal weather forecast models, and find that doing so allows skillful prediction of these oscillations up to 5 weeks, a longer time horizon than if we use the algorithms currently in common use.

Key Points:

- A sliding window, multi-variate EOF analysis identifies spatial structures of tropical intraseasonal oscillations in all the seasons
- Intraseasonal lower-level zonal winds and convection maximize in the winter hemisphere; upper-level winds in summer hemisphere
- A Real-time Multivariate Intraseasonal Index derived from the sliding-window EOFs is skillfully predicted by subseasonal forecast models

Correspondence to:
S. Wang,
wangsg@outlook.com

Citation:
Wang, S., Martin, Z. K., Sobel, A. H., Tippett, M. K., Dias, J., Kiladis, G. N., et al. (2022). A multivariate index for tropical intraseasonal oscillations based on the seasonally-varying modal structures. *Journal of Geophysical Research: Atmospheres*, *127*, e2021JD035961. https://doi.org/10.1029/2021JD035961

Received 30 SEP 2021
Accepted 20 JAN 2022

Author Contributions:
Conceptualization: Shuguang Wang, Zane K. Martin, Adam H. Sobel, Michael K. Tippett, Juliana Dias, George N. Kiladis, Hong-Li Ren, Jie Wu
Data curation: Shuguang Wang, Hong-Li Ren, Jie Wu
Formal analysis: Shuguang Wang
Funding acquisition: Shuguang Wang, Adam H. Sobel, Michael K. Tippett
Investigation: Shuguang Wang
Methodology: Shuguang Wang
Resources: Shuguang Wang
Software: Shuguang Wang
Supervision: Shuguang Wang
Validation: Shuguang Wang
Visualization: Shuguang Wang
Writing – original draft: Shuguang Wang, Zane K. Martin, Adam H. Sobel,

1. Introduction

Tropical intraseasonal oscillations (ISOs), including the canonical Madden-Julian Oscillation (MJO; Li et al., 2018; Madden & Julian, 1971, 1972; Xie et al., 1963), and boreal summer intraseasonal oscillation (BSISO; Krishnamurti & Subramanian, 1982; Yasunari, 1979), exhibit highly complex patterns in time and space, and across seasons. Many authors have recognized that the MJO exhibits a significant seasonal cycle in latitude and amplitude (e.g., Adames et al., 2016; Hendon & Salby, 1994; Jiang et al., 2018; Madden, 1986; Zhang & Dong, 2004). To first order, intraseasonal convection follows the sun, peaking immediately southward of the equator during boreal winter, and northward of the equator during boreal summer (Zhang & Dong, 2004).

Since their discovery, significant effort has been devoted to formally identifying the ISOs in a variety of observational data sets based on eigenvector analysis. While many indices have been developed to represent ISOs, most

Michael K. Tippett, Juliana Dias, George N. Kiladis, Hong-Li Ren, Jie Wu
Writing – review & editing: Shuguang Wang, Zane K. Martin, Adam H. Sobel, Michael K. Tippett, Juliana Dias, George N. Kiladis, Hong-Li Ren, Jie Wu

perform best during one part of the year and have difficulty accurately representing the seasonality of ISOs, with only a few exceptions (e.g., Kikuchi et al., 2012; Kiladis et al., 2014). For instance, some intraseasonal indices use variables averaged in latitude and from all seasons in their eigenvector analysis. As a consequence, the resulting structures are invariant throughout the year. This approach has the benefit of simplicity, but the tradeoff is that the index cannot adequately resolve any seasonally dependent meridionally structure. To represent seasonality, authors often rely on the method of composite analysis. By compositing, variables are grouped and averaged at each phase defined by the ISO indices. Indeed, compositing helps visualize rich zonal and meridional structures associated with ISOs. Nevertheless, compositing has some disadvantages compared to eigenvector analysis. Averaging over the phases, for example, cannot discern whether or not the results are delayed responses to their diabatic heating. By this reasoning, we suggest that it is advantageous to have eigenvectors with seasonally varying spatial structures as in, for example, Kikuchi et al. (2012) and Kiladis et al. (2014).

One purpose of the present study is to find seasonally varying ISO eigenvectors with both meridionally symmetric and antisymmetric components and to build ISO indices from them. Our starting point is the Real-time Multivariate MJO (RMM) index (Wheeler & Hendon, 2004; hereafter referred to as WH04), which is widely used for tracking the MJO. The EOFs for RMM are constant throughout the seasons and have no meridional structure. A key advantage of RMM is that it allows real-time monitoring and forecasting of the MJO, unlike MJO indices that use bandpass filtering. Because of this advantage, RMM is widely regarded as the de facto standard for representing the MJO. Careful examination of the RMM, nevertheless, reveals some limitations, for example conflation of the MJO with equatorial Kelvin waves (Roundy et al., 2009), under-representation of convection relative to wind (Liu et al., 2016; Straub, 2013; Ventrice et al., 2013), and a lack of northward propagation in boreal summer (Wang et al., 2018).

Kikuchi et al. (2012) and Kiladis et al. (2014), hereafter referred to as K14) developed MJO indices based solely on outgoing longwave radiation (OLR), which is a measure of cloudiness often used as a surrogate for rainfall, to address RMM's underrepresentation of convection. A key distinction between RMM and the OLR-based MJO index (OMI) developed in K14, is that OMI explicitly includes meridional structure, whereas RMM does not. The inclusion of meridional structure likely helps to differentiate the ISO from Kelvin waves, as Kelvin waves are theoretically symmetric with respect to the equator for a symmetric basic state (though observed convectively coupled Kelvin waves lack such perfect symmetry, presumably due to basic state asymmetries). While the OMI was designed to track the MJO, Wang et al. (2018) confirmed that the OMI also tracks the BSISO. OMI therefore offers a seasonally unified treatment of ISOs, in contrast to other approaches which use separate indices for summer (BSISO) and winter (MJO; e.g., Kikuchi et al., 2012).

As with the RMM, a real-time version of OMI (ROMI) is available for forecasting and real-time monitoring. Wang et al. (2019) showed that the anomaly correlation skill of ROMI forecasts exceeds 0.6 for lead times up to 35 days in the best current operational forecast model (ECMWF), which is 1 week longer than for RMM forecasts (Vitart, 2017). The higher skill for OMI compared to RMM forecasts is also robust across S2S forecast systems (Wang et al., 2019). Notably, this higher skill for OMI forecasts contradicts the widely perceived notion that convection ought to be less predictable than winds. It is possible that RMM and ROMI represent different aspects of the MJO as a result of their different development methodologies and that the aspect of the MJO represented by the RMM index is less predictable. In part to test this hypothesis, in this study we build upon the methodology used to calculate the OMI and develop a new Multivariable Intraseasonal oscillation Index (MII) which includes winds in addition to OLR.

Since our goal in this study is to identify distinct spatial structures of ISOs in different seasons, we modify the sliding-window EOF method of K14 with a weighted (by day of the year) EOF plus rotation methodology that improves consistency and reduces noise (Wang, 2020). The weighted EOF method is a key aspect because a single EOF analysis across all seasons tends to mix the ISO structures in different seasons, unless meridional structures are ignored (e.g., WH04). As we demonstrate, this approach leads to MII being well-suited for real-time monitoring and forecasts *in all seasons*. Furthermore, despite the fact that MII is developed from data with meridional structure and therefore the data has more than 10 times the number of degrees of freedom as that used in the development of RMM, the fractions of variance explained by the leading EOF spatial structures of MII are significantly larger than those for RMM. Overall, here we show that MII: (a) offers a unified treatment of tropical intraseasonal oscillations (i.e., the MJO and BSISO) in all seasons, and (b) is more predictable by dynamical models than RMM.

The rest of this article is organized as follows. Section 2 introduces the data used, the data preparation steps for computing intraseasonal anomalies, and describes the weighted EOF method. Section 3 contains results from the EOF analysis and discusses some basic properties of the MII index and its application to subseasonal forecasts. Section 4 summarizes this study.

2. Methodology and Datasets

2.1. Datasets

We use the following datasets: for OLR we use NOAA interpolated daily 2.5° resolution data (Liebmann & Smith, 1996), and for zonal winds at 850 hPa (U850) and 200 hPa (U200) we use the ERA5 global reanalysis datasets (Hersbach et al., 2020), in both cases daily from 1979 to 2017. The wind variables are interpolated onto 2.5° horizontal grid, with 144 grid points in longitude (0, 2.5°E, 5°E, …, 357.5°E) and 17 grid points in latitude (20°S, …, 2.5°S, 0, 2.5°N, …, 20°N). Zonal winds from the ECMWF -Interim (Dee et al., 2011) and NCEP reanalysis (Kalnay et al., 1996) were also tested, and the spatial patterns of the EOFs show very minor differences. The insensitivity to the choices of the reanalysis illustrates the robustness of the methodology.

For comparison, the RMM index (WH04), OMI (K14), and the BSISO and MJO indices from Kikuchi et al. (2012), are also examined. The RMM index is constructed based on a real-time filter, as discussed below. In addition, a 20–90 days bandpass filtered RMM index is computed to illustrate the difference between real-time and bandpass-filtered intraseasonal indices. This index, referred to herein as fRMM, is computed by projecting bandpass filtered OLR, U200 and U850 anomalies onto the RMM EOFs, and then normalizing each variable to have standard deviation of one.

2.2. Methodology

We follow the multi-variable approach, as in WH04, using OLR, U850, and U200 to extract the baroclinic structure and convective signature of ISOs. The core of our algorithm is the Empirical Orthogonal Function analysis method (Lorenz, 1956), which is widely used due to its simplicity. Building upon prior knowledge of the MJO, our algorithm is tailored to extract eastward propagating tropical intraseasonal signals. The algorithm used to derive the index is largely the same as K14 and Wang (2020), as summarized in the following paragraphs. Readers uninterested in the technical details may skip this section. We emphasize that while there are multiple steps to derive the sliding-window EOFs as a function of day of the year (DOY), computing the rMII/MII index from the EOFs is nearly as straightforward as RMM, except for the latitude dependance and using EOFs for the corresponding DOY.

The data are first pre-processed in three steps to extract intraseasonal anomalies of zonal wind and OLR before the EOF analysis:

1. Remove the climatology and the first three seasonal harmonics to obtain daily anomalies
2. Apply a 20–96 days bandpass filter to these daily anomalies with a 139-weight, non-recursive Lanczos filter (Duchon, 1979). A zero-phase digital filter (filtfilt; Oppenheim & Schafer, 2010) ensures zero phase shift. Note steps 1 and 2 are applied independently to data at each grid point, that is, independently of latitude and longitude
3. Remove the zonal mean and westward-propagating components by transforming the data into wavenumber-frequency space, setting the Fourier coefficients corresponding to westward propagation to zero, and transforming back to physical space. This step is referred to as the "eastward filter", and is applied separately to data at each latitude

After the pre-processing, we compute the EOFs and then form the index following the steps similar to W20, as summarized as follows:

1. For each day of the year (DOY), denoted T, we generate year-long data chunks centered on T and with super-Gaussian weighting as

$$\hat{F}(t,T,\phi,\lambda) = F(t,\phi,\lambda)exp\left[-\left(\frac{t-T}{60}\right)^4\right] \quad (1)$$

where F is the gridded time series data (i.e., the eastward, bandpass-filtered OLR and wind). T ranges from 0 to 364 and t from −182 to 180. λ and ϕ denote longitude and latitude, respectively. We then concatenate the year-long data chunks to form long time series whose length matches the original data. An important consequence of using the super-Gaussian function is that the resulting EOFs and eigenvalues (discussed below), remain the same even if the data chunks (years) are randomly permuted because time continuity is ensured: this is not the case when a sliding window is used, as in K14.

2. We form a data matrix by combining the window-processed intraseasonal anomalies ($\hat{F}$) for U850, U200 and OLR as: $X = [\mathrm{U850}/\sigma_{\mathrm{U850}}; \mathrm{U200}/\sigma_{\mathrm{U200}}; \mathrm{OLR}/\sigma_{\mathrm{OLR}}]^{\mathrm{T}}$, where σ_{U850} (1.63 m/s), σ_{U200} (4.54 m/s), and σ_{OLR} (12.13 W/m^2) are the areal means of the standard deviations of the variables over all grid points from 20 °S to 20 °N. This step is adopted from WH04. Standard SVD analysis is then performed on the data matrix X to extract the EOF patterns, which appear as degenerate (i.e., not well-separated) pairs that explain the same fraction of variance
3. We rotate the leading EOF pairs to align their zonal structures by applying a rotation matrix with angle θ to the degenerate eigenvector pair (EOF1, EOF2). This may be written as

$$\begin{bmatrix} \mathrm{EOF1}' \\ \mathrm{EOF2}' \end{bmatrix} = \begin{bmatrix} \cos\theta & -\sin\theta \\ \sin\theta & \cos\theta \end{bmatrix} \begin{bmatrix} \mathrm{EOF1} \\ \mathrm{EOF2} \end{bmatrix}, \tag{2}$$

where the primes indicate the EOFs after rotation. The rotation angle θ is a function of T and is chosen to maximize the correlation between the meridional mean of the U850 component here and the U850 component of RMM at each T. There is no specific reason for choosing U850; we tested other options (e.g., by correlating U200 or OLR) and the difference is very minor. Because the rotation matrix is orthonormal, the rotation operation preserves the orthogonality of the EOF pair and the total fraction of variance they explain (W20). This step is necessary to obtain consistent structures at any longitude because the zonal structures of the leading EOFs are not always aligned in longitude throughout the 365 days of the year. We take advantage of the fact that the leading eigenvalue pairs from step 2 are degenerate, and that linear combinations, including the above rotation transformation, remain valid eigen-solutions.

4. We project the 20–96 days bandpass filtered wind and OLR anomalies onto the two rotated EOFs corresponding to the day of the year of the anomalies, forming two time series MII1 and MII2. The resultant multivariate index for tropical intraseasonal oscillations (MII) is the normalized time series resulting from this projection
5. The real-time counterpart of MII is obtained using the same EOFs, but real-time anomalies are projected instead of bandpass filtered anomalies. The real-time anomalies are obtained as follows (similar to Kikuchi et al., 2012 and K14): the mean of the previous 40 days is first subtracted from the anomalies obtained in step 1 of the data processing (i.e., after removing the climatology). These anomalies are then further smoothed using a 9-day running average, where we reduce the number of days in the running average to 7, 5, 3, and 1 at days −4, −3, −2, and −1, respectively. We refer this as "40-9 days real-time filter". The two components of the real-time MII are referenced as rMII1 and rMII2, respectively. Both are normalized to have unit standard deviation

2.3. Frequency Response Functions of the Real-Time Filter

The performance of the real-time filters was tested by Kikuchi et al., 2012 and K14. They showed that the 40-9 days filter yields higher correlations (∼0.9) with the original signals among various filter lengths. Another widely used real-time filter is to subtract the mean of the previous 120 days, which was used to construct the RMM index and differs both in the number of previous days subtracted and in the 9-day centered running average.

To understand these widely used real-time filters, it is instructive to consider their frequency response functions, whose analytic form is given in Appendix A1. Figure 1 shows that the frequency responses from the 40-9 days real-time filter peaks around the frequency ∼0.015 cycle per day (cpd), and the 0.01–0.022 cpd band is selectively amplified, while both lower (including interannual scale) and higher frequency bands are damped. The frequency response from the RMM 120-day real-time filter is also computed. Figure 1b shows that this filter damps the low-frequency inter-annual components but exhibits an undesired peak at 0.005 cpd (∼200 day period). Note that neither is perfect, as both are real-time approximations to the bandpass filter, which needs many more future data

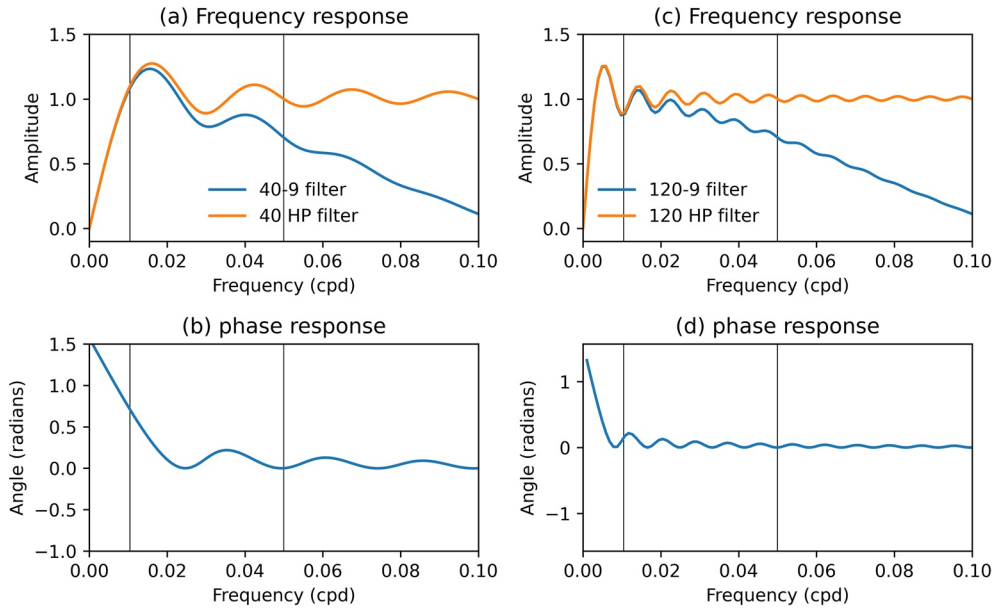

Figure 1. Frequency response function of the real-time filters. (a) Amplitude and (b) phase responses for the 40-9 days filter (blue) and 40-day highpass filter (orange). (c) Amplitude and (d) phase responses for the 120-9 days filter (blue) and 120-day highpass filter (orange).The horizontal axis is frequency (cpd, cycle per day). The two vertical gray bars in each panel indicate the 20 and 96 days frequency band.

points. Still, here we opt for the 40-9 days real-time filter because it yields higher correlation with bandpass filtered signals and selectively amplifies the intraseasonal band.

3. Results

3.1. Modal Structure of the EOFs

The leading EOFs appear in pairs with approximately identical eigenvalues as a result of eastward filtering that excludes both zonal mean (wavenumber 0) and westward-propagating signals. Figure 2 shows that the explained variance of the leading EOFs ranges from 14% in November (with the minimum at DOY 320) to 17.7% in mid-February (the maximum at DOY 55), such that the leading EOF pair explains ~28%–35% of the total variance. The other modes are well-separated from the leading pair, with variances that are well below 5% throughout the year.

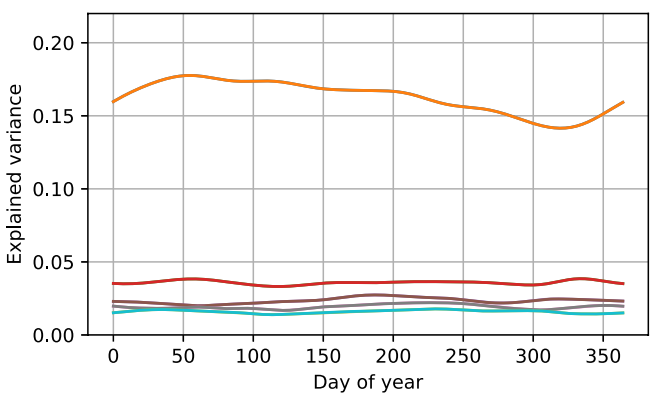

Figure 2. Variance explained by the first five Empirical Orthogonal Function (EOF) pairs as function of day of the year. The orange curve indicates the first pair: EOF1 and EOF2, which overlap with each other because their explained variance is nearly identical. The red, locus, gray and blue curves indicate the rest four EOF pairs.

The leading EOF pairs are functions of latitude, longitude, and day of the year. There are thus 365 EOF pairs for the three variables. Taken together, these display rich spatial and temporal structures, but the amount of information is large. For the sake of brevity in the discussion of seasonal transition in the EOF structures, we will examine the meridional averages.

Figure 3 shows the zonal structure of the meridional averages of the leading EOFs for the three variables averaged over all days. The wind components of both EOFs display a typical baroclinic structure: easterly anomalies at 200 hPa correspond to westerly anomalies at 850 hPa at a given longitude, and vice versa. Convection is nearly in quadrature with winds for EOF2 (Figure 3b): the convective center (OLR minimum) over the Indian Ocean is collocated with the zonal convergence at lower levels and the zonal divergence at upper levels (zero crossings of U850 and U200). For EOF1 (Figure 3a), convection is centered on the Maritime Continent, and its phase is not in quadrature with winds; instead, convection is shifted to the west of the lower level convergence, more in alignment with the westerly winds,

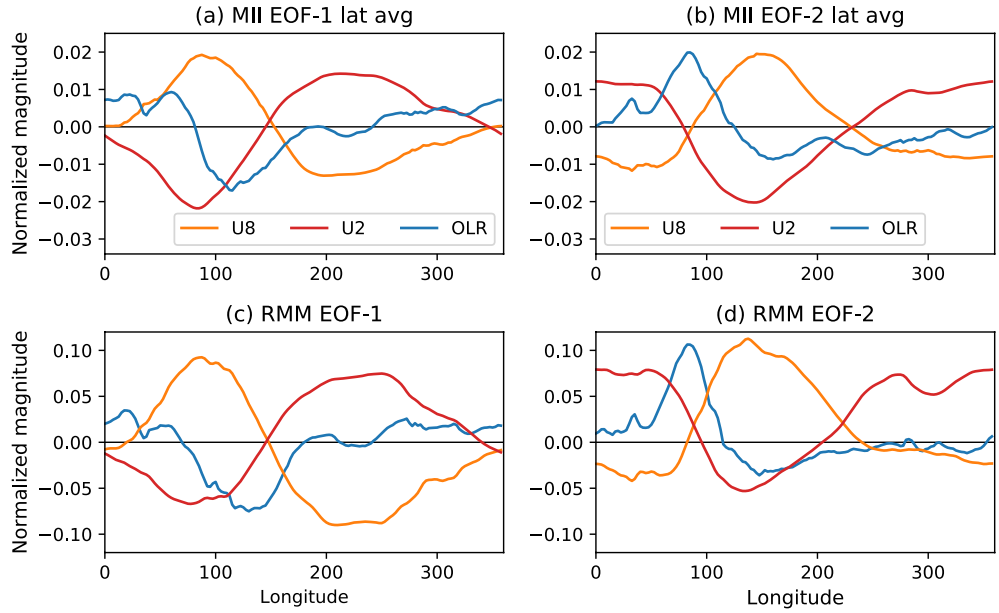

Figure 3. Zonal structures of meridionally averaged Empirical Orthogonal Function for 200 hPa zonal wind (U200), 850 hPa zonal wind (U850) and outgoing longwave radiation (OLR), for the new index MII (top) and RMM (bottom). The variables for the MII index are averaged over all days of the year.

similar to the observed MJO in the Indian Ocean (Zhang, 2005). Still, the nearly quadrature phase relationship between winds and convection across both EOFs is in accord with the well-established notion that the MJO exhibits coupling between large-scale circulation and convection.

The zonal structures of the individual variables compare are similar to those of the familiar RMM EOFs, shown in the bottom panels of Figure 3. The pattern correlation between the two (top and bottom panels in Figure 3) is ∼0.95 for both EOF1 and EOF2. RMM EOF2 has a positive zonal mean in all the variables, because the zonal mean is not removed in its calculation. Inspection of the power spectra of the zonal mean of the RMM-reconstructed zonal winds or OLR indicates the presence of zonal-mean intraseasonal signals, which are signatures of a global wind oscillation in angular momentum as identified in a number of studies (e.g.,Weickmann & Berry, 2009; Weickmann et al., 1992). In contrast, our new EOFs explicitly exclude the zonal mean oscillation found in RMM because eastward filtering removes wavenumber zero.

While the annual mean of the meridional averages for the EOFs is consistent with RMM (Figure 3), the MII EOFs exhibit significant seasonal variability. Figure 4a shows the OLR, U850, and U200 EOFs averaged over latitude, as functions of longitude and time, to illustrate the smooth evolution of the latitudinally symmetric component of the EOFs throughout the year. All three variables change smoothly with DOY, in part as a result of the rotation operation. Seasonal variations in ISO structure can be identified in the amplitudes, and all components are stronger in northern winter. The seasonality is more evident in the antisymmetric components (computed as the difference between averages over the southern and northern latitude bands) of the three variables (Figure 4b). The switch in the sign of all the components around DOYs 100 and 300 indicates the relatively sharp transition between the winter and summer patterns.

Figure 5 shows the full two-dimensional spatial structures of the leading EOFs at DOYs 50 and 200 (19 February and 2 August), taken as representative patterns for boreal winter and summer, respectively. At day 50, OLR and U850 maxima are primarily located over the Indian Ocean, Maritime Continent, and southern Pacific convergence zone (SPCZ), while U200 is less localized, with zonal wavenumber-1 structure. Interestingly, while OLR and U850 are shifted south of the equator in the winter hemisphere, U200 shows more structure in the northern, winter hemisphere.

At day 200, the OLR component exhibits a northwest-southeast tilted structure over the northern Indian Ocean (Figure 5b), South China Sea, and northwest Pacific Ocean. There are also weak signals in the eastern Pacific

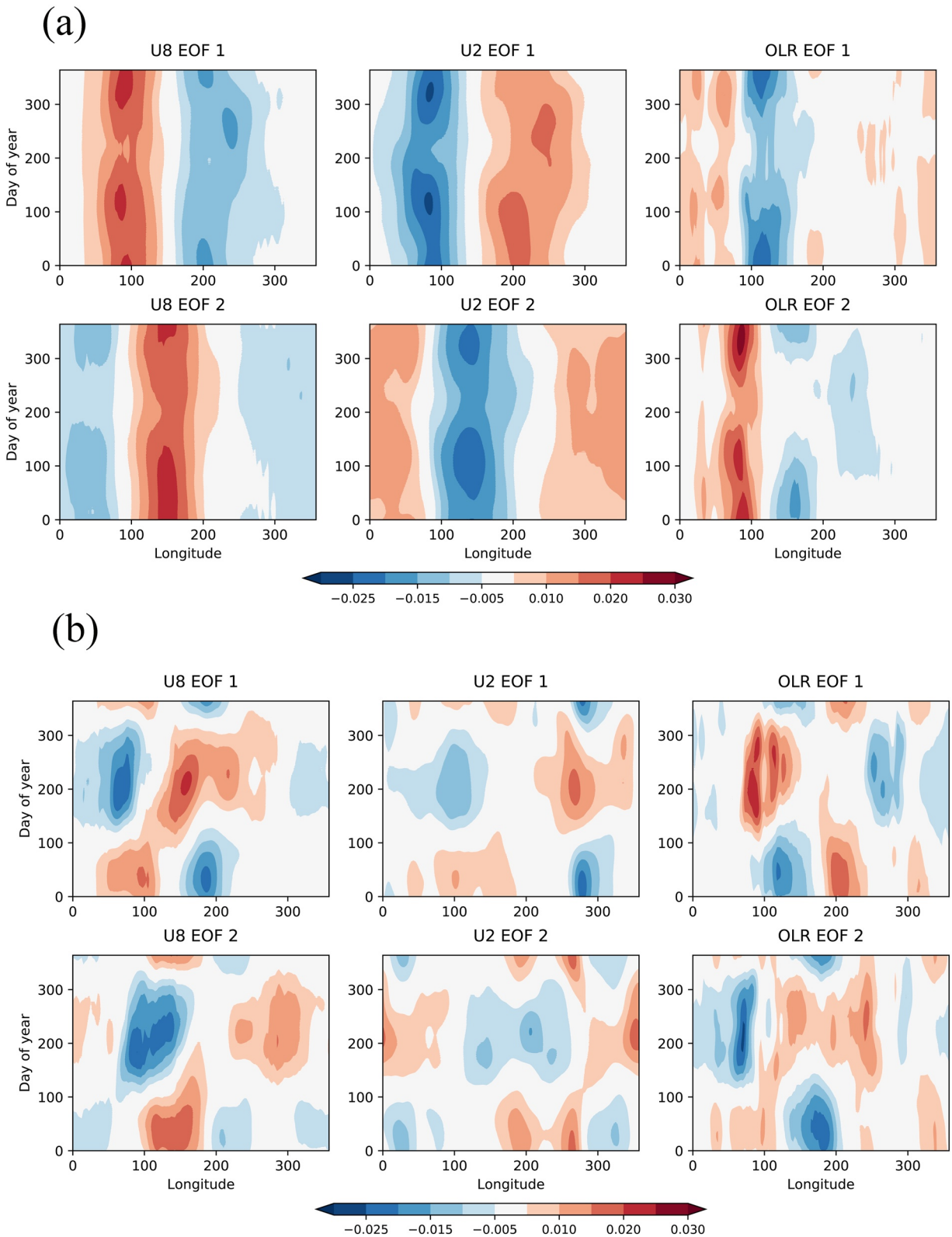

Figure 4. (a) Meridionally symmetric structures of the three variables in EOF1 (top panels) and EOF2 (bottom panels) of the new index MII. (b) As (a) but for antisymmetric structures (i.e., the difference between southern and northern latitudes).

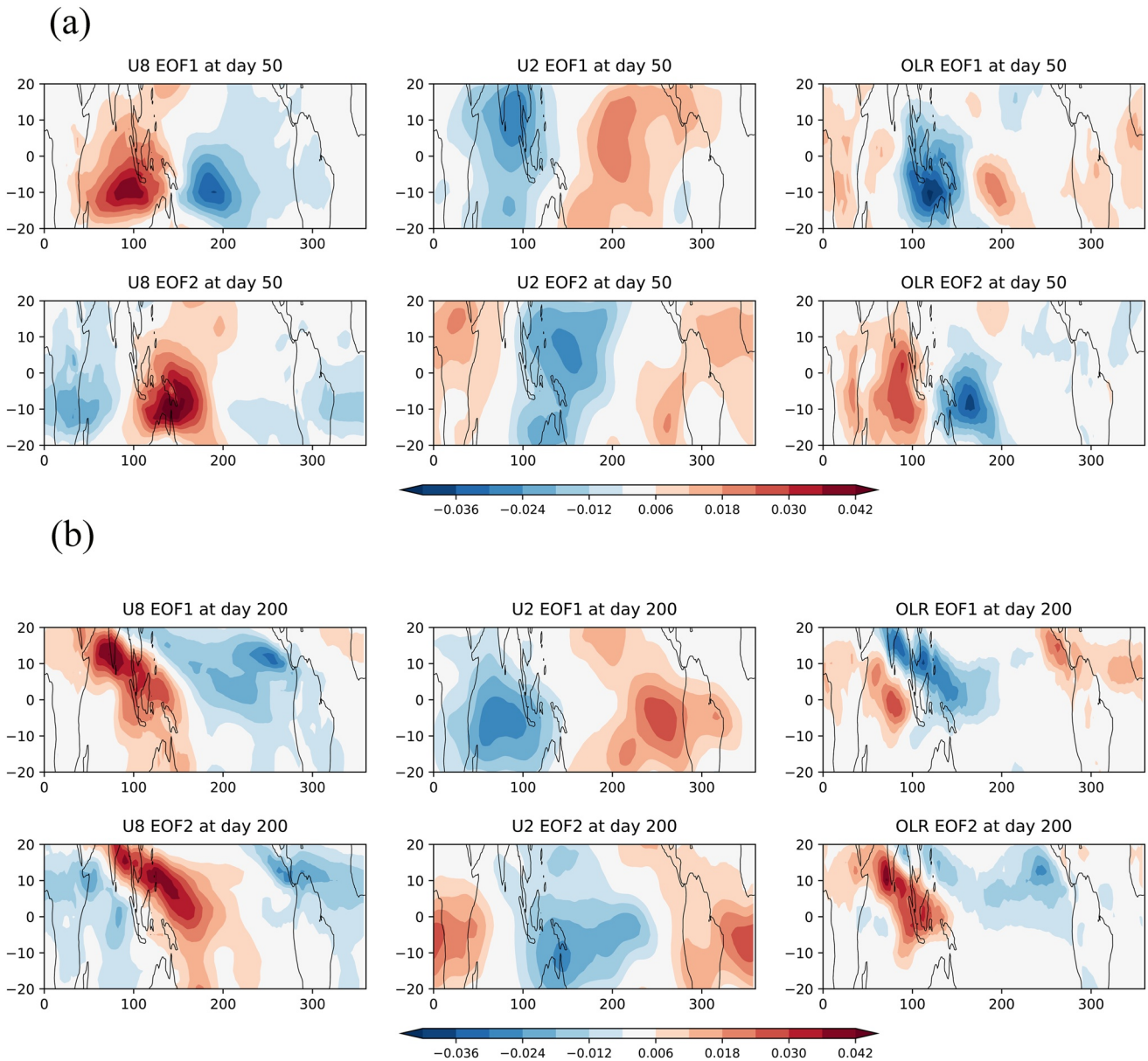

Figure 5. Spatial structures of EOF1 and EOF2 of the new index MII at (a) day 50 and at (b) day 200. U850, U200 and outgoing longwave radiation (OLR) are shown from left to right.

ITCZ region and over the Atlantic Ocean. The northwest-southeast tilted structure is stronger in U850 compared to the other two variables. While the largest values in U850 and OLR are primarily located in the northern hemisphere, the U200 component is shifted toward the southern hemisphere and displays a much less tilted spatial structure.

While the EOF structures discussed above depend on the choice of rotation, the data reconstructed from the EOFs do not, and are the same regardless of the rotation choice. We compute the reconstructed anomalies R as:

$$R(x, y, t) = [\mathrm{MII1(t)} \times \mathrm{EOF1_R}(x, y, T) \times \mathrm{a_1} + \mathrm{MII2(t)} \times \mathrm{EOF2_R}(x, y, T) \times \mathrm{a_2}] \times \sigma_\mathrm{R}$$

where $\mathrm{EOF1/2_R}$ are the corresponding patterns for variable R (U850, U200, or OLR), and T denotes the day-of-year corresponding to time t. MII1/2 are the projections of intraseasonal anomalies onto the leading EOFs, $\mathrm{a_{1,2}}$ are the normalization factors (see Section 2.2, Step 4), and σ_R are the areal means of the standard deviations of the variables (Section 2.2, Step 2).

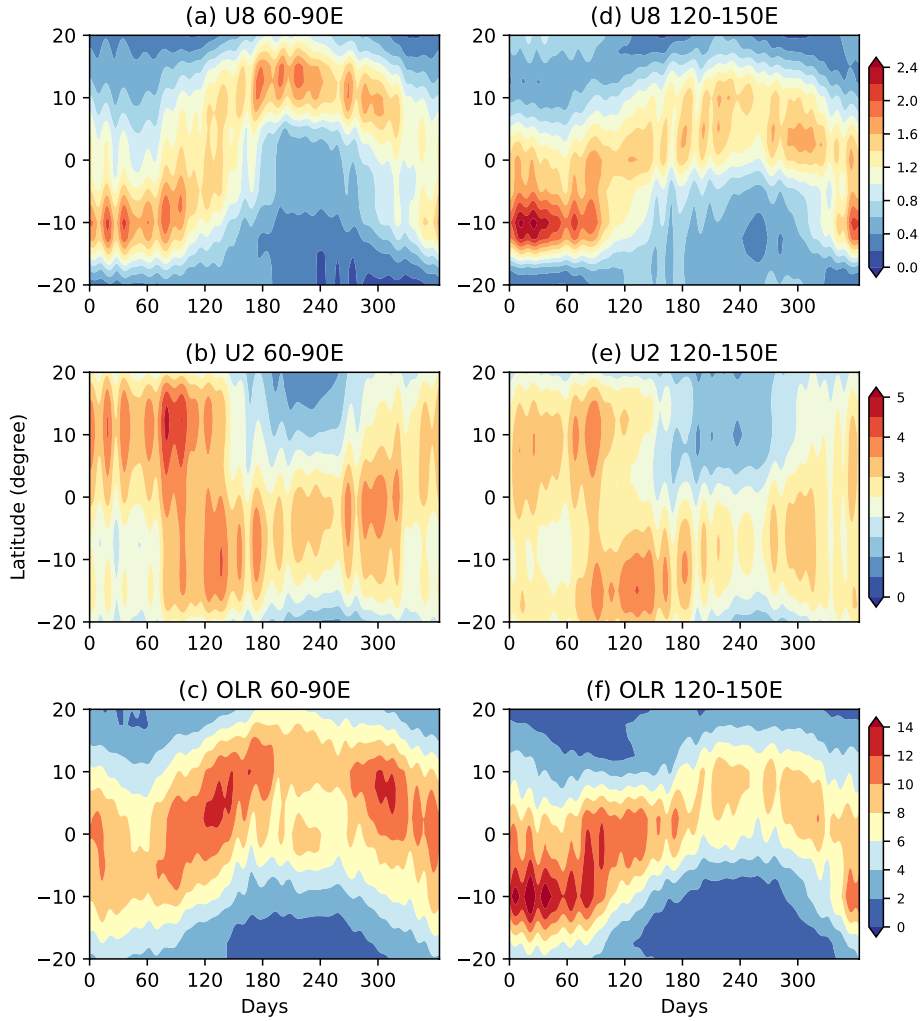

Figure 6. Standard deviation of reconstructed U850 (a, d, m/s), U200 (b, e, m/s), and outgoing longwave radiation (OLR) (c, f, W/m2) anomalies in the Indian Ocean (60–90°E, left column) and western Pacific (120–150°E, right column), as a function of day of year and latitude.

Figure 6 shows the standard deviations of the reconstructed daily U850, U200, and OLR anomalies as functions of latitude and DOY averaged over two longitude bands: 60–90°E and 120–150°E. The contrast in meridional structures between U200 and U850 is consistent with that seen in the spatial EOF structures in Figure 5: U850 and OLR have their largest values in the summer hemisphere, while U200 peaks in the winter hemisphere. Another interesting feature evident in Figure 6 is that the seasonality of individual variables varies with longitude. For example, intraseasonal OLR over the Indian Ocean (Figure 6c) shows peak activity near days 120 and 300 (Figure 6c), while its peak activity in the western Pacific (Figure 6d) occurs around days 0–60 (i.e., northern winter).

The seasonal contrast between the upper and lower tropospheric circulations has been discussed separately in the literature of the MJO. Zhang and Dong (2004) showed that the intraseasonal signals in low-level winds and convection are strongest in the summer hemisphere, while those in upper-level winds are strongest in the winter hemisphere. Also, many studies have noticed that the MJO has a strong impact on northern hemispheric winter weather (e.g., Barlow et al., 2005; Hoell, 2012). It is often tacitly assumed that these upper level features are related to the strong jet stream in the winter hemisphere (e.g., Jin & Hoskins, 1995). Adames et al. (2016) recognized the peculiar hemispheric distribution of the MJO upper and lower level circulations through regression and composite analysis. They loosely referred to the "MJO-related" circulation, and attributed the upper level structure to the time-lagged Rossby wave response to tropical heating, as in Bao and Hartmann (2014). On the

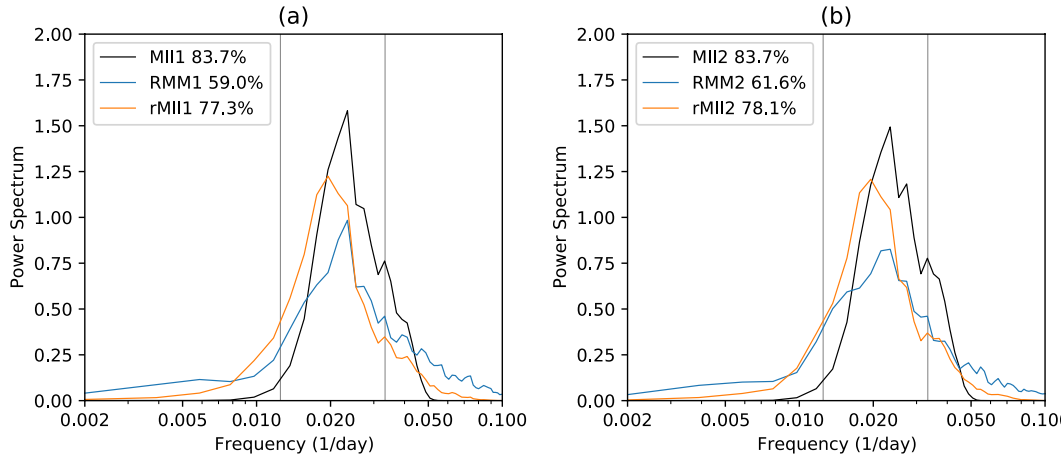

Figure 7. Power spectra of the (a) first and (b) second principal components of MII, rMII, and RMM. Vertical lines indicate the 30–80 days intraseasonal window. The indices are unitless, and the unit of power spectra is 1/(1 day).

other hand, the tropical intraseasonal oscillation may interact with Asian summer monsoon or jet stream during the later boreal summer season (Liu et al., 2020).

Our EOF analysis establishes that the variation in meridional structure with height and season is a feature of the tropical intraseasonal oscillations themselves. One possible explanation could be that the stronger response at upper levels is consistent with the observation that the cross-equatorial Hadley circulation is strongest toward the winter hemisphere (e.g., Held & Hou, 1980). Strong meridional outflow toward the winter hemisphere will lead to a stronger response there because of the Rossby wave source in the winter hemisphere with a stronger extratropical jet (Sardeshmukh & Hoskins, 1988). On the other hand, an alternative interpretation is that the upper-level structure may arise from the resonance between the tropical intraseasonal oscillations and planetary-scale intraseasonal baroclinicity in the extratropics (Straus & Lindzen, 2000). There is no time delay between the upper level feature and the heating in this view, unlike the delayed Rossby wave response. We do not pursue this issue in the present study, as our focus here is on development of a new MJO index, but we recommend this issue be examined further in future work using numerical experiments that appropriately control the climatology of extratropical jets (e.g., Ma & Kuang, 2016; Tulich & Kiladis, 2021).

3.2. Properties of the MII Index

Prior studies (Straub, 2013; Ventrice et al., 2013) have noted that the RMM index weights circulation variables more heavily than it weights OLR; OLR contributes only around ∼14.7% to the total variance. The contributions of the three variables (U200, U850, and OLR) to MII may also be evaluated the same manner. As with RMM, we find that the individual variables do not contribute equally to the total variance of MII: the variances associated with for U850, U200, and OLR, respectively, are ∼38%, 37%, and 25%. Still, the contribution of OLR to MII is substantially higher than in RMM (14.7%, Ventrice et al., 2013), indicating that MII is more balanced between circulation and OLR variables. Approaches to further balance the contributions of different variables (e.g., scaling each variable differently, as discussed in Liu et al., 2016 & Liu, 2019) could be explored in future work.

We further examine the power spectra of MII compared to other indices. Figure 7 shows the power spectra of the two principal components of the MII, rMII, and RMM indices. We compute the fractions of total variance in the intraseasonal band (here defined as 30–80 days for consistency with WH04) for MII1 and MII2 (the first two principal components) from 1979 to 2016. For MII we find that this fraction is 0.84 for both MII1 and MII2. These values are significantly higher than those for RMM, which are 0.59 for RMM1 and 0.62 for RMM2 (note quoted values are slightly different from Figure 2 of WH04 due to the different periods). For the real time MII (rMII), the spectra notably shift to lower frequency due to the real-time filtering (see Appendix) which peaks at 0.015 cpd. The fraction of intraseasonal power in rMII is 0.77 for rMII1 and 0.78 for rMII2: slightly less than for MII, but still significantly higher than for RMM. RMM also has a significantly higher fraction of its variance at higher (>0.05 days^{-1}) and lower frequencies (<0.006 days^{-1}). Consistent with the power spectra, RMM tends to

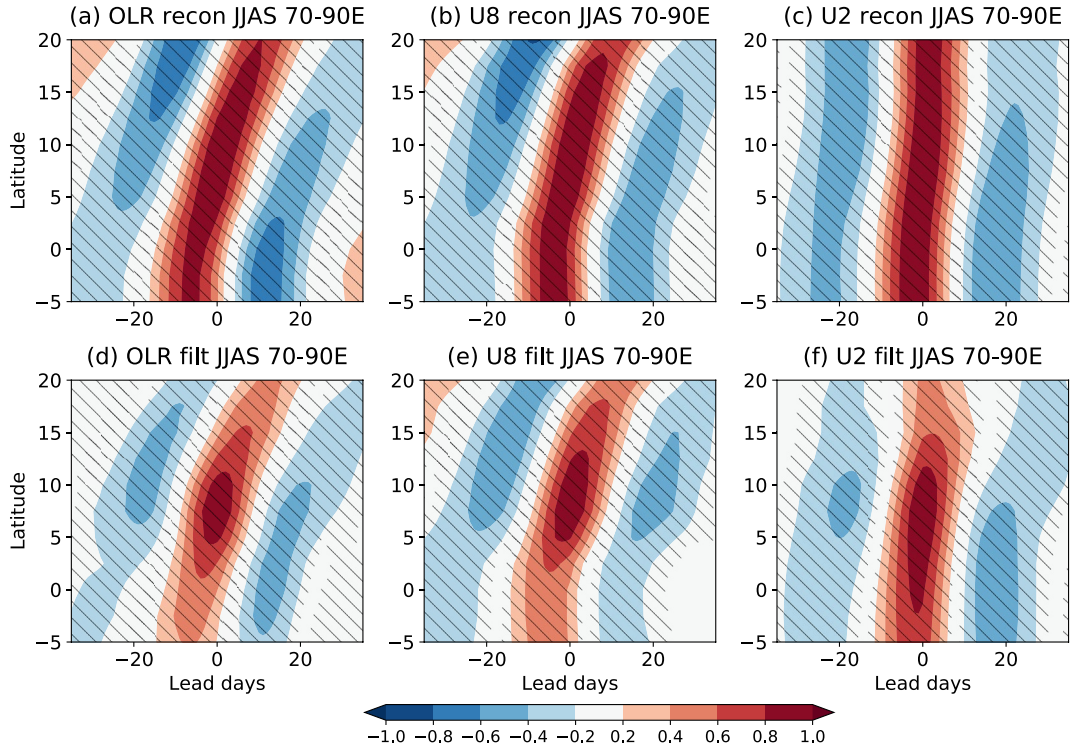

Figure 8. Top: lag correlation coefficient of MII reconstructed U850 (a), U200 (b), and outgoing longwave radiation (c) anomalies averaged 5–10°N and 70–90°E in summer (June to September) against the same reconstructed anomalies averaged 0–5°N. Bottom row as top, but for bandpass filtered (10–90 days) anomalies. Hatches indicate correlation coefficients that are significantly nonzero at the 0.01 level.

be noisy and shows significant day-to-day variations, as is often observed in the phase diagrams (e.g., Figure 9 in the next section).

An important aspect of an ISO index is its amplitude, usually computed as sqrt ($R1^2 + R2^2$), where R1 and R2 are the two components of the index. This quantity is widely used for distinguishing between strong and weak ISO events, so it is useful to understand its statistical distribution. Both R1 and R2 are normalized to have unit variance, such that they are both independant normally distributed variable. As a result, the amplitude follows the Chi distribution χ_2, where the subscript indicates the degree of freedom (2). From a statistics table or function in standard mathematical software (e.g., scipy.stats.chi in Python3), it is straightforward to compute the probability distribution. For example, the commonly used amplitude value 1 corresponds to 39.3% cumulative probability, while amplitude value 1.177 corresponds to 50%.

3.3. Propagation Characteristics

ISOs, as defined here, propagate eastward in all seasons. During boreal summer, they often propagate poleward (northward in the northern hemisphere) as well (Lawrence & Webster, 2002; Wang & Rui, 1990). Nevertheless, some EOF-based intraseasonal oscillation indices fail to capture this northward propagation (Wang et al., 2018). Here we examine the meridional propagation in different variables using lag correlation.

The top panels of Figure 8 show the lag correlation of the reconstructed U850, U200 and OLR anomalies averaged over 70–90°E, as functions of latitude and time, against the corresponding anomalies over the reference area 5–10°N, 70–90°E. A northward propagation speed of ~1° per day is evident in U850 and OLR, but no comparable northward propagation can be seen in U200. This lack of meridional propagation in U200 is surprising. To confirm that it is a real feature in the data, we compute the same lag correlation for the 20–96 days band-pass filtered anomalies of each variable, without using any reconstruction with indices (bottom panels of Figure 8). The band-pass filtered data shows the same northward propagation in low-level zonal wind and OLR, but as

Table 1
Bivariate Correlation Between Daily MII and Three Other Intraseasonal Indices During the Period From 1980 to 2016 for the Boreal Winter (December–February) and Summer (June–August)

	Dec–Feb			June–Aug		
	RMM	OMI	K12-MJO	RMM	OMI	K12-BSISO
MII	0.80 (0)	0.89 (−1)	0.90 (0)	0.76 (−2)	0.80 (−3)	0.80 (−3)
OMI	0.75 (1)	–	0.90 (1)	0.63 (2)	–	0.86 (1)
RMM	–	0.75 (−1)	0.73 (0)	–	0.62 (-2)	0.58 (−1)

Note. The time lag of highest correlation is shown in the bracket (positive values: the index in the left columns leads that in the top row).

above lacks any northward propagation in 200 hPa zonal wind. The overall finding is thus similar to the lag-correlation pattern from the reconstructed anomalies, albeit with less coherence due to noise. This result affirms that the EOF results are representative of the signals in the unfiltered data, and we infer that the lack of northward propagation in upper-level zonal wind is a real physical feature of the northern summer oscillation.

3.4. Comparison With Other Indices

The correlation between MII and other MJO indices ranges from 0.58 to 0.9, depending on index and season (Table 1). The correlation with RMM is ∼0.80 at day −1 in boreal winter (DJF), and 0.76 at day −2 in summer (JJA). The MII-OMI correlation is 0.89 in winter at day −1, and 0.80 in summer at day −3. The correlation between MII and K12's MJO index is 0.90 at day 0, 0.80 between MII and K12's BSISO index. The correlations between OMI and RMM are notably lower than these values in both seasons.

By design, RMM identifies the MJO using intraseasonal anomalies that are computed without bandpass filtering, since such filtering relies on past and future values. One way to see how much information is lost in this approach is to compare RMM with fRMM, which projects bandpass-filtered data onto the RMM EOFs. The fRMM index also, to some extent, facilitates comparison of RMM to OMI and MII: both OMI and MII use filtered data projected onto their EOFs. OMI and MII also have real-time counterparts (ROMI and rMII) which are similar to RMM in that they use unfiltered data projected onto their EOFs.

The bivariate correlation between fRMM and RMM is ∼0.8 from 1979 to 2016. If we use this as a measure for the degree of approximation of RMM to the intraseasonal MJO, it is notably lower for fRMM than OMI or MII. For both OMI and MII, correlation between the standard index and its real-time counterpart is ∼0.9. One interpretation of this difference is that the spatial filtering that arises from projecting onto the 2-D OMI and MII patterns is more effective at removing variance outside the ISO timescale than is projecting on to the RMM EOFs. This is likely because the OMI/MII EOFs vary by day of the year, and thus more accurately match the seasonal ISO variability, compared to the RMM patterns, which mix the summer and winter spatial structures.

3.5. The DYNAMO Case

In addition to overall measures of index performance, we further examined how the MII represents specific MJO events. We focus on those observed during the Dynamics of the Madden–Julian Oscillation (DYNAMO) field campaign in 2011–2012 (Yoneyama et al., 2013; Zhang et al., 2013). Figure 9 shows MII, its real-time counterpart, RMM, and fRMM during the DYNAMO period from October 2011 to March 2012. Compared to RMM, both MII and rMII are significantly smoother, which is desirable to the extent that we prefer that synoptic (day-to-day) noise be largely absent in an index representing intraseasonal oscillations.

The October MJO event during DYNAMO was characterized by circumglobal circulation anomalies (Gottschalck et al., 2013). In contrast, convection anomalies associated with the October MJO event started in the Indian Ocean in the middle of October 2011 (Sobel et al., 2014; Wang et al., 2015, 2016; Yoneyama et al., 2013). Despite the initiation of a convective signal only in mid-October, the RMM index showed relatively high amplitude before mid-October, followed by a decrease to below one once the MJO entered the Indian Ocean basin (Phase 2; see Figure 9c). It is desirable that an MJO index, even one primarily associated with circulation,

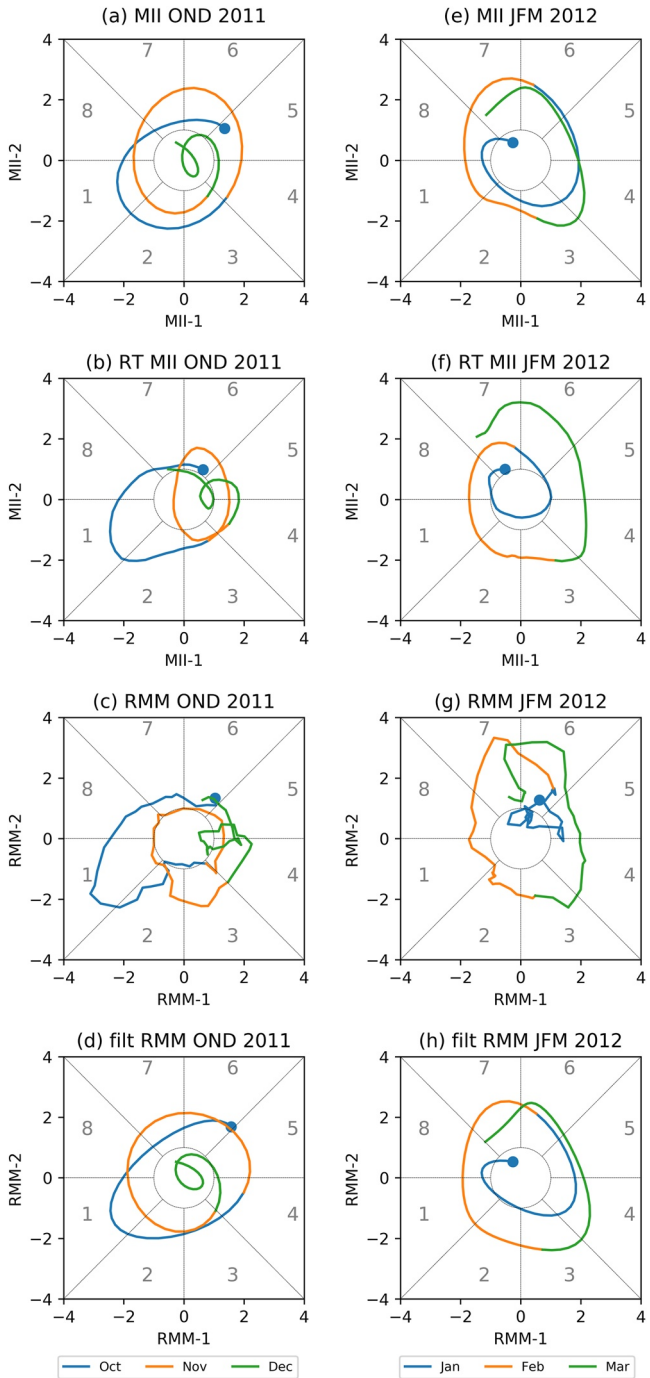

Figure 9. Left column: phase diagrams of MII, rMII, RMM, and fRMM from October to December 2011 during the DYNAMO period. Right column: as in left column but for the period January–March 2012. The blue dots denote the start dates: 1 October 2011 (left column) and 1 January 2012 (right column). The phase number is noted in gray. Here the phase diagram follows the convention established by WH04: phases 2-3 represents the MJO is active in the Indian Ocean; phases 4-5, Maritime Continent; phases 6-7, western Pacific; phases 8-1, western hemisphere and Africa.

be able to correctly capture the MJO's convective initialization. While RMM depicted a sharp drop of the MJO amplitude to below 1 during this period, the amplitude of both MII and rMII remained greater than 1 throughout October 2011. The MII index completed a full cycle during November, while the rMII had small values in the western hemisphere.

Identification of the December MJO event was more ambiguous (Gottschalk et al., 2010), as its characteristics were not typical of the MJO. The RMM values were greater than 1 during most of December, whereas other indices were greater than 1 during the first half of December and smaller than 1 during the second half of that month. Viewed through the MII index, the MJO completed a full cycle in January 2012 in rMII with amplitude greater than 1. This behavior is similar to that represented by the OMI index (Figure 6d of K14) and fRMM, but the signature in January is very unclear in RMM. In contrast, the February and March MJO events were both large in amplitude and completed slightly more than half a cycle during each month: these features were captured by all four indices considered here.

Careful comparison between the phase diagrams for the two filtered indices, MII and fRMM, during the DYNAMO period indicates that they are quite similar during this period. This is not a coincidence, as the bivariate correlation between MII and fRMM reaches ~0.96 from 1979 to 2016, which is much higher than the MII-RMM correlation (Table 1). This suggests that fRMM may also be used similarly to MII in practice, though we emphasize that the physical underpinnings—such as the spatial patterns and EOF structures—are very different for MII and fRMM.

4. Application to the S2S Reforecasts

One important application of intraseasonal oscillation indices is real-time tracking and monitoring, as illustrated in the preceding discussion of the DYNAMO case and Figure 9. Yet another key application of an ISO index is its use in numerical forecasts, as ISO indices help evaluate model performance in predicting the ISOs. In this section, we compute the real-time MII from output from the European Centre for Medium-Range Weather Forecasts (ECMWF), National Centers for Environmental Prediction (NCEP) CFSv2, and China Meteorological Administration (CMA) version 1 (Beijing Climate Center Climate System Model 1.2, BCC-CSM1.2, Wu et al., 2014; Wu et al., 2020) and version 2 (BCC-CSM2-High Resolution, BCC-CSM2-HR, Wu et al., 2021), as part of the WMO/S2S reforecast data set (Vitart et al., 2017). The CMAv2 (BCC-CSM1.2) was a major upgrade of CMAv1 (BCC-CSM2-HR) in that model resolution is greatly improved, and the reforecasts switched from the fixed scheme to the "on-the-fly" approach for the past 15 years since November 2019. Further technical details may be found at the S2S Wikipedia: https://confluence.ecmwf.int/display/S2S/CMA+model+description.

Wang et al. (2019) showed that there is prediction skill for MJO convection at lead times up to 35 days for the ECMWF model, and 28 days for the CFSv2 model, based on the maximum lead time at which the bivariate correlation coefficient between the forecast and observed real-time OMI exceeds 0.6. This is 5–10 days greater than for RMM (Kim et al., 2018; Lim et al., 2018; Vitart, 2017). This result was unexpected, because convection is generally perceived to be less predictable than the circulation pattern represented by RMM. Here we investigate this issue further.

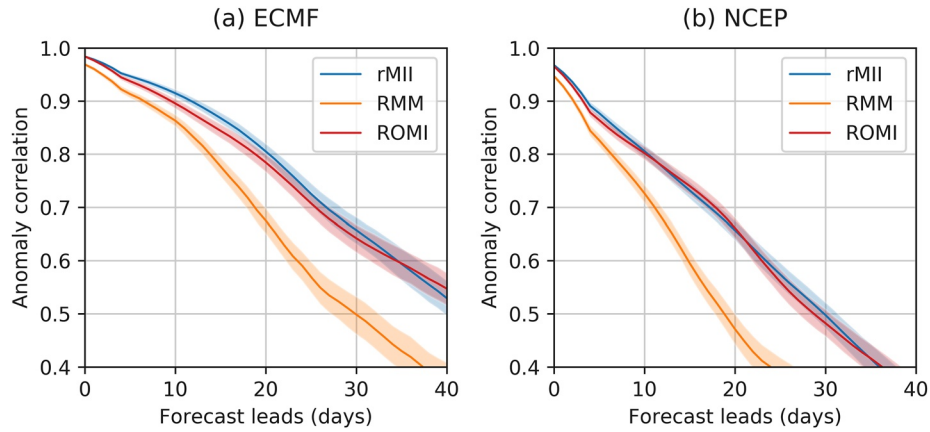

Figure 10. Bivariate correlation of forecast rMII, ROMI, and RMM in the extended boreal winter (DJFM), using the ECMWF (left) and NCEP CFSv2 (right) models. The shaded region indicates the 95% confidence interval.

The bivariate correlation skill of rMII, ROMI, and RMM is computed as a function of forecast lead days for the reforecasts from ECMWF and NCEP CFSv2 models (Wang et al., 2014) from 1999 to 2010, as: $COR = \frac{\sum_i \mathbf{F}_i \cdot \mathbf{O}_i}{\sqrt{\sum_i |\mathbf{F}_i|^2}\sqrt{\sum_i |\mathbf{O}_i|^2}}$, where **F** and **O** be forecast and observed ISO indices. **F** and **O** are vectors with two components (F1, F2) and (O1, O2) for forecasts and observations, respectively, and i denotes the index of the (re)forecasts. Here $i < N$, and N is the total number of forecasts. The number of reforecasts is 840 and 1,452 for ECMWF and NCEP CFSv2, respectively, from December to March during this period. The confidence interval of the reforecast skill is assessed based on the bootstrap resampling method (Wilks, 2011). The reforecasts are resampled 10,000 times to generate the statistical distribution from which the upper and lower 2.5% is computed. If there is no overlap between the confidence intervals (2.5%, 97.5%) of two skills at the same lead, it is considered that the two are statistically different.

The forecasted ROMI and rMII are computed the same manner as in Wang et al. (2019). First, forecast OLR, U200 and U850 anomalies are calculated with respect to the lead-dependent reforecast climatology of each model. Second, we prepend the past 40 days of observed OLR and/or wind anomalies to the reforecasts. The forecast OLR anomalies are interpolated to the 2.5° grid of the EOFs, and projected onto the day-of-the-year dependent eigenfunctions of OLR from K14 for ROMI, or the corresponding eigenfunctions for rMII. Data from four future days are used for the running average or forecasts at the current date. Near the end of the reforecast, the number of days is reduced in the running average to 7, 5, 3, and 1 at days −4, −3, −2, and −1 of the reforecasts, respectively.

Figure 10 shows the rMII bivariate skill as a function of lead time during the extended winter (December to March). Judging prediction skill based on the threshold value COR = 0.6: rMII skill reaches 34 days for ECMWF, and 23 days for CFSv2. The ROMI prediction skill is comparable to, or slightly less than that of rMII for both models, whereas for RMM prediction skill is 24 days for ECMWF, and 15 days for CFSv2 for COR = 0.6. These values are similar to those in Vitart, 2017, see their Figure 1b), but nearly 10 days less than for rMII or ROMI. The difference between the two is statistically significant based on the confidence intervals from the resampling method. Note the behavior is not sensitive to the choice of COR threshold—COR values for rMII at other lead days are also significantly higher than those for RMM.

These results indicate that RMM underestimates the MJO prediction skill compared to rMII, and it is useful to consider why the rMII may have higher prediction skill than RMM. There are several differences between RMM and rMII: (a) the 40-day versus 120-day real-time filter, (b) the 9-day smoothing for rMII, and (c) the spatial structure of the EOFs: in particular the meridional structure of MII/rMII reduces synoptic noises (e.g., Figure 7) due to, for example, convectively coupled Kelvin waves (Roundy et al., 2009). This may make the underlying intraseasonal spatial structures (EOFs) more predictable. One may also argue that the skill gain using the rMII is due to 9-day smoothing, which reduces synoptic noises and extends predictability, or due to the 40-9 days real-time filter. We test these arguments by applying the same 9-day smoothing to the RMM index, that is, using

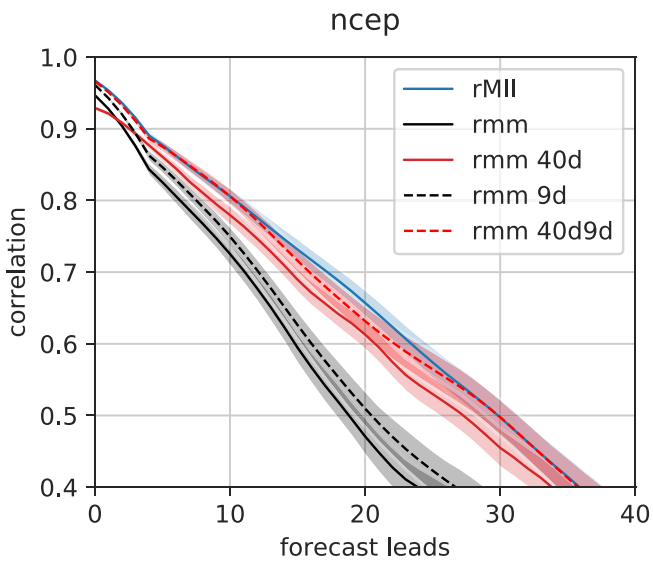

Figure 11. Prediction skill of rMII (blue solid), standard RMM (black solid), RMM with 9-day smoothing (black dashed), RMM with a real-time 40-day filter (red), RMM with a real-time 40-9 days filter (red dashed). The shaded region indicates the 95% confidence interval.

a 120-9 days real-time filter, as well as using a 40-9 days filter for RMM, and assess skill performance with the reforecast data from the NCEP CFSv2 model.

Comparing the black solid and black dashed curves in Figure 11 indicates that the prediction skill gain from the 9-day smoothing is small and not statistically significant, by ~2–3 days for the NCEP model at threshold value COR = 0.5 or 0.6. This shows that the skill gain using rMII is not due to the simple 9-day smoothing. We further test the 40-day filter (red solid), which increases the skill by 5–6 days compared to RMM. Finally, applying the 40–9 real-time filter to RMM in the winter season (red dashed in Figure 11) increases the skill to the extent nearly comparable to the rMII (blue), except in the region COR 0.6–0.7. This substantial skill gain is consistent with the frequency response function shown in Figure 1 that the 40-9 days filter selectively amplifies the intraseasonal signals, and Figure 7 that the fraction of the explained variance reduces synoptic noise and shifts to lower intraseasonal bands.

The S2S models are updated continuously, and a successful MJO index should be able to assess and track model improvement in representation of the MJO. To assess this, we use the CMA reforecasts to examine the impact of model version on the MJO prediction skill measured by rMII. Figure 12 shows the rMII bivariate skill for CMA v1 and v2 as a function of lead time during the extended winter and summer seasons. The improvement due to model upgrade is significant. The rMII skill is 22 days for v1 and 27 days in winter for v2 using the threshold COR = 0.6; 16 days for v1 and 22 days for v2 in summer. The results suggest that CMA v2 has improved MJO prediction by 5 days across the seasons, and the skill of rMII is about 10 days longer than that of the RMM index in CMA v1 when compared to the results of previous studies (Wu et al., 2016; Wu & Jin, 2021). It is also useful to compare the prediction skill in the two seasons (Figure 12b): the skill is less in summer than in winter.

5. Conclusions

We have developed an all-season, multivariate index for tropical intraseasonal oscillations, including the MJO and BSISO, based on an EOF analysis of zonal winds at 200 and 850 hPa and OLR. The new index captures the seasonality of the ISO using a weighted EOF analysis of intraseasonal anomalies, following the methodology of Kiladis et al. (2014) and Wang (2020).

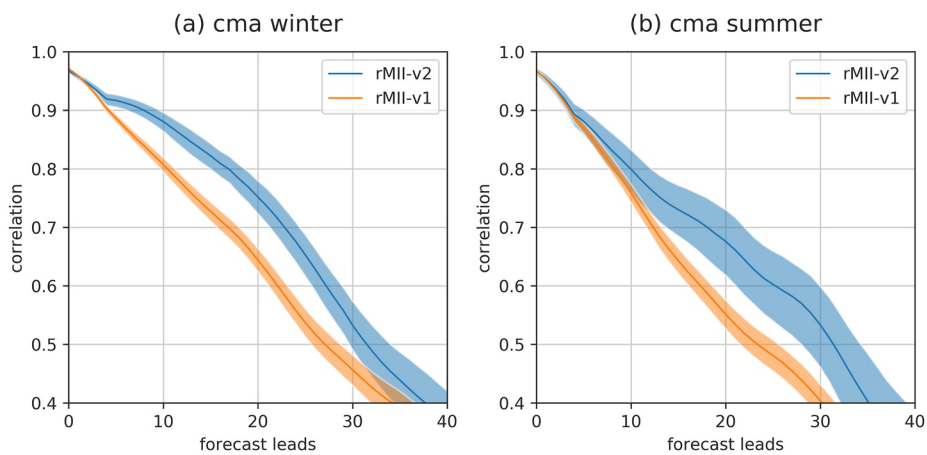

Figure 12. Bivariate correlation of forecast rMII in the extended boreal winter (a) and summer seasons (b) for China Metrological Administration (CMA) v1 and v2. The shaded region indicates the 95% confidence interval.

The meridionally symmetric structures of the resulting EOFs are consistent with those in WH04, and the phase relationship among the zonal winds and OLR supports the well-established notion that the MJO is a consequence of circulation-convection coupling. On the other hand, the antisymmetric component of wind and OLR is more complex. The EOFs exhibit rich meridional structures which vary with season and altitude. The lower level wind and OLR are more localized and primarily located in the summer hemisphere, whereas the upper level wind is shifted toward the winter hemisphere. The shift is not expected given the convection is centered in the summer hemisphere. This complex structure arises naturally out of the EOF analysis, suggesting that it should be thought as an intrinsic element of the modal structure of tropical intraseasonal oscillations. This is different from the conventional view that the upper level feature may be considered as the Rossby wave response to tropical heating in the winter hemisphere because of the presence of the extratropical jet stream. Pursuing an explanation of the upper-level feature may be useful for improved understanding of the ISOs.

Compared to the widely used RMM index, the all-season multivariate ISO index, MII, contains significantly less synoptic noise. The intraseasonal variance is ∼77% of the total power spectrum for either of the two leading principal components, while the RMM has ∼60% in the intraseasonal range by the same definition. The real-time version of this index, rMII, is constructed by using 9-point averaging and shows a bivariate correlation to MII of ∼0.9. This is comparable with the correlation between OMI and ROMI, or correlation between the BSISO index and its real-time counterpart by Kikuchi et al. (2012). Similar measures can also be estimated for RMM: projecting 20–90 days bandpass filtered anomalies onto the RMM EOFs yields two time series (fRMM), which have a lower correlation with RMM (∼0.8) compared to other indices.

Application of the real-time MII index to three models participating in the WMO/S2S reforecast datasets – the ECMWF, the NCEP CFSv2, and the CMA version 1 and 2 models – shows that the prediction skill for MII is ∼10 days longer than that for the RMM index during the boreal winter season, and comparable to the MJO convection prediction skill represented by ROMI. Based on the frequency response function and additional analysis of model prediction skill, it is shown that the RMM prediction skill may be improved if the same 40-9 days real-time filter is used. This implies that switching from the conventional 120-day real-time filter to a 40-9 days filter would improve RMM prediction skill for the boreal winter MJO. On the other hand, it is well known that RMM is less effective at representing intraseasonal oscillations in boreal summer, because the BSISO exhibits significant meridional structure and poleward propagation which the RMM excludes due to its dependence only on longitude and time. Our diagnosis indicates that MIIs can distinguish this seasonality due to its seasonally varying EOFs.

Finally, we suggest that seasonality is of fundamental importance for understanding the intraseasonal oscillations. Recent observational analysis and numerical simulations (Adames et al., 2016; Jiang et al., 2018; Wang et al., 2021) indicate that moisture plays a crucial role in the BSISO, similar to the boreal winter. Wang and Sobel (2022) proposed a parsimonious moisture mode theory for the seasonality of the intraseasonal oscillations. Their model displays distinct meridional structure and propagation due to change in meridional moisture gradient corresponding to different seasons, although both are highly idealized. Taken together, these studies articulate the view that the MJO and BSISO belong to the same moisture mode family, and the MII index is consistent with this view. We suggest that the new index developed here may be used to track the intraseasonal oscillations in real time, across the seasons, in a consistent and unified manner.

Appendix A: Frequency Response Function of the Real-Time Filter

Here we derive the frequency response function of the real-time filters. The 40-9 days filter consists of two steps: (a) subtract the mean of the previous 40 days from the anomalies, and (b) smooth the results for step 1 using a 9-day running average. These two steps are both linear filtering operations: the first one is a high-pass filter, and the second one is a low-pass filter. We give the frequency response function of the 40-day (step 1) and the 9-day (step 2) filter, separately. The equation for a finite impulse response filter (FIR, e.g., Oppenheim & Schafer, 2010) may be written as:

$$y[n] = \sum_{k=0}^{N} b_k x[n-k] \tag{A1}$$

where N is the order of the filter, x [i] is the discrete input signal, and y [i] is the output. The coefficient for the 40-day real-time filter ($N = 40$) is written as:

$$b = [1, -1/N, -1/N, \ldots, -1/N] \tag{A2}$$

where the term $-1/N$ is repeated N times. Assuming single wave input as $Ae^{i\omega n}$, where A is the amplitude and n is the time step (in the unit of days here), frequency response is defined as the ratio between the output y and the input $Ae^{i\omega n}$. Substitution of this single wave and b yields the frequency response H_N as:

$$\begin{aligned} H_N(\omega) &= \sum_{k=0}^{N} b_k e^{-i\omega k} \\ &= 1 - \frac{1}{N}\sum_{k=1}^{N} e^{-i\omega k} \\ &= 1 - \frac{\sin[\omega(N+1)/2]}{(N+1)\sin(\omega/2)} e^{-i\omega(N+2)2} \end{aligned} \tag{A3}$$

The 40-day filter is H_{40}, and the 120-day filter may be written as H_{120}. The second term in the right hand side is due to averaging of previous N days. The expression A3 is a complex number. Its absolute value indicates amplitude responses, while the angle indicates phase.

For the 9-day running average filter, the coefficient is b = [1/9, 1/9, …, 1/9]. Its frequency response may be written as:

$$H_{a9}(\omega) = \frac{\sin(9\omega/2)}{9\sin(\omega/2)} \tag{A4}$$

Because running mean is centered, H_9 is real, and phase shift is zero. Taking both linear filters together, the frequency response of the 40-9 days real-time filter is the product of H_{40} and H_{a9},

$$H(\omega) = H_{40}H_{a9} = \left\{1 - \frac{\sin[41\omega/2]}{41\sin(\omega/2)} e^{-i\omega 21}\right\} \frac{\sin(9\omega/2)}{9\sin(\omega/2)} \tag{A5}$$

The magnitude of $H(\omega)$ is shown in Figure 1. $H(\omega)$ may also be solved numerically using the freqz function in Python or Matlab, which yields identical curves to numerical evaluation of the analytic form $H(\omega)$.

Data Availability Statement

The MII index and the Python code to produce it are available at https://doi.org/10.5281/zenodo.5806377. The MJO RMM index is available at: http://www.bom.gov.au/climate/mjo/. The ERA5 Reanalysis is available at https://doi.org/10.5065/D6X34W69, Research Data Archive at the National Center for Atmospheric Research, Computational and Information Systems Laboratory, Boulder, Colo. The NOAA Interpolated Outgoing Longwave Radiation is available from https://psl.noaa.gov/data/gridded/data.interp_OLR.html. Python based routines for calculating the OMI using reanalysis or model data are discussed in Hoffmann et al. (2021) and available at: https://doi.org/10.5281/zenodo.3613752. The S2S datasets are available at https://apps.ecmwf.int/datasets/data/s2s-reforecasts-instantaneous-accum-ecmf/levtype=sfc/type=cf/. The MII index and the code are also available upon request from the corresponding author.

Acknowledgments
We thank five anonymous reviewers for their insightful comments that greatly helped to improve the ideas and presentation of this study. Shuguang Wang acknowledges support from NSF AGS-1543932 and NSFC 41875066. Adam H. Sobel acknowledge support from the Office of Naval Research Award N00014-16-1-3073. Zane K. Martin acknowledges support from the National Science Foundation under Award No. 2020305.

References

Adames, Á. F., Wallace, J. M., & Monteiro, J. M. (2016). Seasonality of the structure and propagation characteristics of the MJO. *Journal of the Atmospheric Sciences*, *73*, 3511–3526. https://doi.org/10.1175/JAS-D-15-0232.1

Bao, M., & Hartmann, D. L. (2014). The response to MJO-like forcing in a nonlinear shallow-water model. *Geophysical Research Letters*, *41*, 1322–1328, https://doi.org/10.1002/2013GL057683

Barlow, M., Wheeler, M., Lyon, B., & Cullen, H. (2005). Modulation of daily precipitation over southwest Asia by the Madden–Julian oscillation. *Monthly Weather Review*, *133*(12), 3579–3594.

Dee, D. P., Uppala, S. M., Simmons, A. J., Berrisford, P., Poli, P., Kobayashi, S., et al. (2011). The ERA-Interim reanalysis: Configuration and performance of the data assimilation system. *Quarterly Journal of Royal Meteorological Society*, *137*, 553–597. https://doi.org/10.1002/qj.828

Duchon, C. E. (1979). Lanczos filtering in one and two dimensions. *Journal of Applied Meteorology*, *18*, 1016–1022. https://doi.org/10.1175/1520-0450(1979)018<1016:LFIOAT>2.0

Gottschalck, J., Roundy, P. E., Schreck, C. J., III, Vintzileos, A., & Zhang, C. (2013). Large-scale Atmospheric and Oceanic conditions during the 2011–12 DYNAMO field campaign. *Monthly Weather Review*, *141*(12), 4173–4196. https://doi.org/10.1175/mwr-d-13-00022.1

Gottschalck, J., Wheeler, M., Weickmann, K., Vitart, F., Savage, N., Lin, H., et al. (2010). A framework for assessing operational Madden—Julian oscillation forecasts. *Bulletin of the American Meteorological Society*, *91*(9), 1247–1258. https://doi.org/10.1175/2010bams2816.1

Held, I. M., & Hou, A. Y. (1980). Nonlinear axially symmetric circulations in a nearly inviscid atmosphere. *Journal of the Atmospheric Sciences*, *37*(3), 515–533.

Hendon, H. H., & Salby, M. L. (1994). The life cycle of the Madden–Julian oscillation. *Journal of the Atmospheric Sciences*, *51*(15), 2225–2237.

Hersbach, H., Bell, B., Berrisford, P., Hirahara, S., Horányi, A., Muñoz-Sabater, J., et al. (2020). The ERA5 global reanalysis. *Quarterly Journal of the Royal Meteorological Society*, *146*(730), 1999–2049. https://doi.org/10.1002/qj.3803

Hoell, A., Barlow, M., & Saini, R. (2012). The leading pattern of intraseasonal and interannual Indian Ocean precipitation variability and its relationship with Asian circulation during the boreal cold season. *Journal of Climate*, *25*(21), 7509–7526.

Hoffmann, C. G., Kiladis, G. N., Gehne, M., & von Savigny, C. (2021). A Python Package to Calculate the OLR-Based Index of the Madden-Julian-Oscillation (OMI) in Climate Science and Weather Forecasting. *Journal of Open Research Software*, *9*. https://doi.org/10.5334/jors.331

Jiang, X., Adames, A. F., Zhao, M., Waliser, D., & Maloney, E. (2018). A unified moisture mode framework for seasonality of the Madden–Julian oscillation. *Journal of Climate*, *31*(11), 4215–4224. https://doi.org/10.1175/JCLI-D-17-0671.1

Jin, F., & Hoskins, B. J. (1995). The direct response to tropical heating in a baroclinic atmosphere. *Journal of the Atmospheric Sciences*, *52*(3), 307–319.

Kalnay, E., Kanamitsu, M., Kistler, R., Collins, W., Deaven, D., Gandin, L., et al. (1996). The NCEP/NCAR 40-Year reanalysis project. *Bulletin of the American Meteorological Society*, *77*(3), 437–471. https://doi.org/10.1175/1520-0477(1996)077<0437:tnyrp>2.0.co;2

Kiladis, G. N., Dias, J., Straub, K. H., Wheeler, M. C., Tulich, S. N., Kikuchi, K., et al. (2014). A comparison of OLR and circulation-based indices for tracking the MJO. *Monthly Weather Review*, *142*, 1697–1715. https://doi.org/10.1175/MWR-D-13-00301.1

Kikuchi, K., Wang, B., & Kajikawa, Y. (2012). Bimodal representation of the tropical intraseasonal oscillation. *Climate Dynamics*, *38*, 1989. https://doi.org/10.1007/s00382-011-1159-1

Kim, H., Vitart, F., & Waliser, D. E. (2018). Prediction of the Madden–Julian oscillation: A review. *Journal of Climate*, *31*(23), 9425–9443.

Krishnamurti, T. N., & Subramanian, D. (1982). The 30-50 day mode at 850 mb during MONEX. *Journal of the Atmospheric Sciences*, *39*(9), 2088–2095. https://doi.org/10.1175/1520-0469(1982)039<2088:tdmamd>2.0.co;2

Lawrence, D. M., & Webster, P. J. (2002). The boreal summer intraseasonal oscillation: Relationship between northward and eastward Movement of convection. *Journal of the Atmospheric Sciences*, *59*(9), 1593–1606. https://doi.org/10.1175/1520-0469(2002)059<1593:TBSIOR>2.0.co;2

Liebmann, B., & Smith, C. A. (1996). Description of a complete (interpolated) outgoing long-wave radiation dataset. *Bulletin of the American Meteorological Society*, *77*, 1275–1277.

Lim, Y., Son, S., & Kim, D. (2018). MJO prediction skill of the subseasonal-to-seasonal prediction models. *Journal of Climate*, *31*, 4075–4094. https://doi.org/10.1175/JCLI-D-17-0545.1

Li, T., Wang, L., Peng, M., Wang, B., Zhang, C., Lau, W., & Kuo, H. (2018). A paper on the tropical intraseasonal oscillation published in 1963 in a Chinese Journal. *Bulletin of the American Meteorological Society*, *99*(9), 1765–1779. https://doi.org/10.1175/BAMS-D-17-0216.1

Liu, F., Ouyang, Y., Wang, B., Yang, J., Ling, J., & Hsu, P.-C. (2020). Seasonal evolution of the intraseasonal variability of China summer precipitation. *Climate Dynamics*, *54*(11–12), 4641–4655. https://doi.org/10.1007/s00382-020-05251-0

Liu, P. (2019). MJO evolution and predictability disclosed by the RMM variant with balanced MJO variance in convection and zonal winds. *Climate Dynamics*, *52*, 2529–2543.

Liu, P., Zhang, Q., Zhang, C., Zhu, Y., Khairoutdinov, M., Kim, H., et al. (2016). A revised real-time Multivariate MJO index. *Monthly Weather Review*, *144*(2), 627–642. https://doi.org/10.1175/mwr-d-15-0237.1

Lorenz, E. N. (1956). *Empirical Orthogonal Functions and Statistical Weather Prediction* Scientific Report (Vol. 1, p. 52). Massachusetts Institute of Technology, Department of Meteorology.

Madden, R. A. (1986). Seasonal variations of the 40–50 Day oscillation in the tropics. *Journal of the Atmospheric Sciences*, *43*(24), 3138–3158. https://doi.org/10.1175/1520-0469(1986)043<3138:svotdo>2.0.co;2

Madden, R. A., & Julian, P. R. (1971). Detection of a 40–50 day oscillation in the zonal wind in the tropical Pacific. *Journal of the Atmospheric Sciences*, *28*, 702–708

Madden, R. A., & Julian, P. R. (1972). Description of global-scale circulation cells in the tropics with a 40–50 day period. *Journal of the Atmospheric Sciences*, *29*(6), 1109–1123. https://doi.org/10.1175/1520-0469(1972)029<1109:dogscc>2.0.co;2

Ma, D., & Kuang, Z. (2016). A mechanism-denial study on the Madden-Julian Oscillation with reduced interference from mean state changes. *Geophysical Research Letters*, *43*, 2989–2997. https://doi.org/10.1002/2016GL067702

Oppenheim, A. V., & Schafer, R. W. (2010). *Discrete-time signal processing* (3rd ed., pp. 1–1108). Pearson Higher Education Inc.

Roundy, P. E., Schreck, C. J., Janiga, M. A. (2009). Contributions of convectively coupled equatorial Rossby waves and Kelvin waves to the real-time multivariate MJO Indices. *Monthly Weather Review*, *137*(1), 469–478. https://doi.org/10.1175/2008mwr2595.1

Sardeshmukh, P. D., & Hoskins, B. J. (1988). The generation of global rotational flow by steady idealized tropical divergence. *Journal of the Atmospheric Sciences*, *45*(7), 1228–1251.

Sobel, A. H., Wang, S., & Kim, D. (2014). Moist static energy budget of the MJO during DYNAMO. *Journal of the Atmospheric Sciences*, *71*(11), 4276–4291. https://doi.org/10.1175/jas-d-14-0052.1

Straub, K. H. (2013). MJO initiation in the real-time multivariate MJO index. *Journal of Climate*, *26*, 1130–1151. https://doi.org/10.1175/JCLI-D-12-00074.1

Straus, D. M., & Lindzen, R. S. (2000). Planetary-scale baroclinic instability and the MJO. *Journal of the Atmospheric Sciences*, *57*(21), 3609–3626.

Tulich, S. N., & Kiladis, G. N. (2021). On the regionality of moist Kelvin waves and the MJO: The critical role of the background zonal flow. *Journal of Advances in Modeling Earth Systems*, *13*, e2021MS002528. https://doi.org/10.1029/2021MS002528

Ventrice, M. J., Wheeler, M. C., Hendon, H. H., Schreck, C. J., Thorncroft, C. D., & Kiladis, G. N. (2013). A Modified multivariate Madden–Julian oscillation index using velocity potential. *Monthly Weather Review*, *141*, 4197–4210. https://doi.org/10.1175/MWR-D-12-00327.1

Vitart, F. (2017). Madden—Julian Oscillation prediction and teleconnections in the S2S database. *Quarterly Journal of the Royal Meteorological Society*, *143*, 2210–2220. https://doi.org/10.1002/qj.3079

Vitart, F., Ardilouze, C., Bonet, A., Brookshaw, A., Chen, M., Codorean, C., et al. (2017). The subseasonal to seasonal (S2S) prediction project database. *Bulletin of the American Meteorological Society*, *98*(1), 163–173. https://doi.org/10.1175/BAMS-D-16-0017.1

Wang, B., & Rui, H. (1990). Synoptic climatology of transient tropical intraseasonal convection anomalies: 1975–1985. *Meteorology and Atmospheric Physics*, *44*(1), 43–61.

Wang, S. (2020). A precipitation-based index for tropical intraseasonal oscillations. *Journal of Climate*, *33*(3), 805–823.
Wang, S., Ma, D., Sobel, A. H., & Tippett, M. K. (2018). Propagation characteristics of BSISO indices. *Geophysical Research Letters*, *45*, 9934–9943. https://doi.org/10.1029/2018GL078321
Wang, S., & Sobel, A. H. (2022). A unified moisture mode theory for the Madden–Julian Oscillation and the Boreal Summer Intraseasonal Oscillation. *Journal of Climate*. *35*(4), 1267–1291. https://doi.org/10.1175/JCLI-D-21-0361.1
Wang, S., Sobel, A. H., Lee, C.-Y., Ma, D., Chen, S., Curcic, M., & Pullen, J. (2021). Propagating mechanisms of the 2016 summer BSISO event: Air-sea coupling, vorticity, and moisture. *Journal of Geophysical Research: Atmospheres*, *126*, e2020JD033284. https://doi.org/10.1029/2020JD033284
Wang, S., Sobel, A. H., & Nie, J. (2016). Modeling the MJO in a cloud-resolving model with parameterized large-scale dynamics: Vertical structure, radiation, and horizontal advection of dry air. *Journal of Advances in Modeling Earth Systems*, *8*. https://doi.org/10.1002/2015MS000529
Wang, S., Sobel, A. H., Tippett, M. K., & Vitart, F. (2019). Prediction and predictability of tropical intraseasonal convection: seasonal dependence and the Maritime Continent prediction barrier. *Climate. Dynamics*. *52*(9–10), 6015–6031. https://doi.org/10.1007/s00382-018-4492-9
Wang, S., Sobel, A. H., Zhang, F., Sun, Q., Yue, Y., & Zhou, L. (2015). Regional simulation of the October and November MJO events observed during the CINDY/DYNAMO field campaign at gray zone resolution. *Journal of Climate*, *28*(6), 2097–2119. https://doi.org/10.1175/jcli-d-14-00294.1
Wang, W., Hung, M. P., Weaver, S. J., Kumar, A., & Fu, X. (2014). MJO prediction in the NCEP climate forecast system version 2. *Climate Dynamics*, *42*, 2509–2520.
Weickmann, K., & Berry, E. (2009). The tropical Madden–Julian oscillation and the global wind oscillation. *Monthly Weather Review*, *137*, 1601–1614. https://doi.org/10.1175/2008MWR2686.1
Weickmann, K. M., Khalsa, S. J. S., & Eischeid, J. (1992). The atmospheric angular momentum cycle during the tropical Madden–Julian oscillation. *Monthly Weather Review*, *120*(10), 2252–2263. https://doi.org/10.1175/1520-0493(1992)120<2252:taamcd>2.0.co;2
Wheeler, M. C., & Hendon, H. H. (2004). An all-season real-time multivariate MJO index: Development of an index for monitoring and prediction. *Monthly Weather Review*, *132*, 1917–1932.
Wilks, D. S. (2011). *Statistical methods in the atmospheric sciences*. International Geophysics (3rd ed., pp. 1–676). Academic Press.
Wu, J., & Jin, F.-F. (2021). Improving the MJO forecast of S2S operation models by correcting their biases in linear dynamics. *Geophysical Research Letters*, *48*, e2020GL091930. https://doi.org/10.1029/2020GL091930
Wu, J., Ren, H.-L., Lu, B., Zhang, P., Zhao, C., & Liu, X. (2020). Effects of moisture initialization on MJO and its teleconnection prediction in BCC subseasonal coupled model. *Journal of Geophysical Research: Atmospheres*, *125*(1), e2019JD031537. https://doi.org/10.1029/2019JD031537
Wu, J., Ren, H.-L., Zuo, J., Zhao, C., Chen, L., & Li, Q. (2016). MJO prediction skill, predictability, and teleconnection impacts in the Beijing climate center atmospheric general circulation model. *Dynamics of Atmospheres and Oceans*, *75*, 78–90. https://doi.org/10.1016/j.dynatmoce.2016.06.001
Wu, T., Song, L., Li, W., Wang, Z., Zhang, H., Xin, X., et al. (2014). An overview of BCC climate system model development and application for climate change studies. *Acta Meteorologica Sinica*, *28*(1), 34–56. https://doi.org/10.1007/s13351-014-3041-7
Wu, T., Yu, R., Lu, Y., Jie, W., Fang, Y., Zhang, J., et al. (2021). BCC-CSM2-HR: A high-resolution version of the Beijing climate center climate system model, *Geoscientific Model Development*, *14*, 2977–3006. https://doi.org/10.5194/gmd-14-2977-2021
Xie, Y.-B., Chen, S.-J., Zhang, I.-L., & Hung, Y.-L. (1963). A preliminarily statistic and synoptic study about the basic currents over southeastern Asia and the initiation of typhoon. *Acta Meteorologica Sinica*, *33*(No. 2), 206–217.
Yasunari, T. (1979). Cloudiness fluctuations associated with the northern hemisphere summer monsoon. *Journal of the Meteorological Society of Japan. Ser. II*, *57*(3), 227–242. https://doi.org/10.2151/jmsj1965.57.3_227
Yoneyama, K., Zhang, C., & Long, C. N. (2013). Tracking pulses of the Madden-Julian oscillation. *Bulletin of the American Meteorological Society*, *94*(12), 1871–1891. https://doi.org/10.1175/BAMS-D-12-00157.1
Zhang, C. (2005). Madden-julian oscillation. *Reviews of Geophysics*, *43*, RG2003. https://doi.org/10.1029/2004RG000158
Zhang, C., & Dong, M. (2004). Seasonality in the Madden–Julian oscillation. *Journal of Climate*, *17*(16), 3169–3180. https://doi.org/10.1175/1520-0442(2004)017<3169:SITMO>2.0
Zhang, C., Gottschalck, J., Maloney, E. D., Moncrieff, M. W., Vitart, F., Waliser, D. E., et al. (2013). Cracking the MJO nut. *Geophysical Research Letters*, *40*, 1223–1230. https://doi.org/10.1002/grl.50244